



## Article

# Selective Laser-Assisted Direct Synthesis of MoS<sub>2</sub> for Graphene/MoS<sub>2</sub> Schottky Junction

Min Ji Jeon <sup>1</sup>, Seok-Ki Hyeong <sup>2</sup>, Hee Yoon Jang <sup>1</sup>, Jihun Mun <sup>3</sup>, Tae-Wook Kim <sup>4,5</sup>, Sukang Bae <sup>2,5,\*</sup> and Seung-Ki Lee <sup>1,\*</sup>

<sup>1</sup> School of Material Science and Engineering, Pusan National University, Busan 46241, Republic of Korea; minji@pusan.ac.kr (M.J.J.)

<sup>2</sup> Institute of Advanced Composite Materials, Korea Institute of Science and Technology, Wanju 55324, Republic of Korea

<sup>3</sup> Advanced Instrumentation Institute, Korea Research Institute of Standards and Science, Daejeon 34113, Republic of Korea

<sup>4</sup> Department of Flexible and Printable Electronics, Jeonbuk National University, Jeonju-si 54896, Republic of Korea

<sup>5</sup> Department of JBNU-KIST Industry-Academia Convergence Research, Jeonbuk National University, Jeonju-si 54896, Republic of Korea

\* Correspondence: sbae@kist.re.kr (S.B.); ifriend@pusan.ac.kr (S.-K.L.); Tel.: +82-63-219-8158 (S.B.); +82-51-510-2999 (S.-K.L.)

**Abstract:** Implementing a heterostructure by vertically stacking two-dimensional semiconductors is necessary for responding to various requirements in the future of semiconductor technology. However, the chemical-vapor deposition method, which is an existing two-dimensional (2D) material-processing method, inevitably causes heat damage to surrounding materials essential for functionality because of its high synthesis temperature. Therefore, the heterojunction of a 2D material that directly synthesized MoS<sub>2</sub> on graphene using a laser-based photothermal reaction at room temperature was studied. The key to the photothermal-reaction mechanism is the difference in the photothermal absorption coefficients of the materials. The device in which graphene and MoS<sub>2</sub> were vertically stacked using a laser-based photothermal reaction demonstrated its potential application as a photodetector that responds to light and its stability against cycling. The laser-based photothermal-reaction method for 2D materials will be further applied to various fields, such as transparent display electrodes, photodetectors, and solar cells, in the future.

**Keywords:** selective laser annealing; graphene; molybdenum disulfide (MoS<sub>2</sub>); photothermal reaction; heterostructure; photodetector



**Citation:** Jeon, M.J.; Hyeong, S.-K.; Jang, H.Y.; Mun, J.; Kim, T.-W.; Bae, S.; Lee, S.-K. Selective Laser-Assisted Direct Synthesis of MoS<sub>2</sub> for Graphene/MoS<sub>2</sub> Schottky Junction. *Nanomaterials* **2023**, *13*, 2937. <https://doi.org/10.3390/nano13222937>

Academic Editors: Qijin Cheng and Jian Zhou

Received: 3 October 2023

Revised: 8 November 2023

Accepted: 10 November 2023

Published: 13 November 2023



**Copyright:** © 2023 by the authors. Licensee MDPI, Basel, Switzerland. This article is an open access article distributed under the terms and conditions of the Creative Commons Attribution (CC BY) license (<https://creativecommons.org/licenses/by/4.0/>).

## 1. Introduction

With the development of next-generation devices and the introduction of new functionalities, the primary objective for semiconductor technology is to increase integration density while achieving various form factors through downscaling and ultra-thinning techniques [1–3]. Pioneering research has highlighted the potential of thinning traditional materials such as silicon and oxide semiconductors to improve mechanical flexibility without compromising their quality; however, the innate three-dimensional (3D) crystalline structures of class materials imply inevitable limits to continuous downscaling strategies owing to several challenges such as increased surface energy, quantum effect-induced property changes, and thermal instability. In contrast, 2D crystalline materials, characterized by atomic interconnections in a 2D lattice, inherently retain their electrical, mechanical, and physical properties, even at the atomic scale [4,5]. For these reasons, they have attracted considerable attention as potential core materials for future electronic devices [6]. Notably, these 2D materials are highly compatible [7] with traditional Si-based complementary

metal-oxide semiconductor (CMOS) manufacturing processes, leading to promising results in devices with hybrid structures [8,9].

Methods such as metal-organic chemical-vapor deposition (MOCVD), molecular-beam epitaxy, and atomic layer deposition have led to significant progress in the synthesis of transition-metal dichalcogenides, which are representative 2D semiconductors, on various substrates [10–13]. Even though these methods achieve high-quality materials capable of synthesizing single crystals or controlling the number of layers at the wafer scale, they rely on high synthesis temperatures ( $>700\text{ }^{\circ}\text{C}$ ) [14,15], post-thermal treatments, or specific substrates. Such dependence inevitably necessitates a transfer to the target substrate post-synthesis. Unfortunately, this transfer process typically results in unforeseen chemical contamination, physical wrinkles, and damage, making the prediction of the post-transfer quality and uniformity of the synthesized materials [16,17] increasingly challenging. To this end, laser-assisted synthesis methodologies have been proposed as potential solutions to overcome the limitations of conventional techniques [18–22]. Because of the monochromatic, coherent, and collimated nature of laser sources, photothermal reactions on materials can be systemically controlled by selectively [23–26] inducing lattice vibrations. This allows targeted thermal annealing even when the device chip comprises thermally fragile parts. In this context, the effectiveness of laser-assisted synthesis has been proven through research on the selective synthesis of 2D materials using lasers or the partial modulation of the interface properties of electronics [20–22]. Moreover, significant findings are emerging, demonstrating the direct synthesis of 2D heterostructures beyond the scope of individual materials [27–31]: This is accomplished by integrating distinct 2D materials, particularly n-type  $\text{MoS}_2$  with p-type  $\text{WS}_2$ , eliminating the need for a transfer process. Therefore, various heterojunction structures based on 2D materials need to be implemented and validated by exploiting the universal applicability of selective-laser photothermal reactions.

Herein, we implement a graphene/ $\text{MoS}_2$  heterojunction structure by integrating n-type  $\text{MoS}_2$  on semi-metallic graphene via a laser-assisted selective photothermal-reaction method by optimizing the photothermal and laser parameters. For the synthesis of  $\text{MoS}_2$ , a thermally decomposable  $(\text{NH}_4)_2\text{MoS}_4$  precursor was mixed with an organic solvent, and a fiber laser ( $\lambda = 1.06\text{ }\mu\text{m}$ ) with a high absorption rate for the  $\text{MoS}_2$  precursor was selected to prevent damage to the underlying graphene and substrate. Unlike the traditional CVD synthesis method, controlling the thermal-spreading range using the laser parameters suppressed damage to the surrounding layers, such as the underlying graphene and  $\text{SiO}_2/\text{Si}$  wafer, which provided a means to implement a graphene/ $\text{MoS}_2$ -based photodetector with a robust interface.

## 2. Experimental Section

### 2.1. Materials

Poly(methylmethacrylate) ( $(\text{C}_5\text{O}_2\text{H}_8)_n$ ; PMMA), ammonium tetrathiomolybdate ( $(\text{NH}_4)_2\text{MoS}_4$ ), CAS No. 15060-55-6), and hexamethyldisilazane( $(\text{CH}_3)_3\text{SiNHSi}(\text{CH}_3)_3$ , CAS No. 999-97-3) were purchased from Sigma-Aldrich (St. Louis, MI, USA). A photoresist (AZ 5214-E; PR, LOT NO. USAW417063) and Developer (AZ 300 MIF developer, LOT NO. KR387425) were purchased from Merck (Rahway, NJ, USA). Dimethyl sulfoxide ( $(\text{CH}_3)_2\text{SO}$ , CAS No. 67-68-5) and ammonium persulfate( $(\text{NH}_4)_2\text{S}_2\text{O}_8$ , CAS No. 7727-54-0) were purchased from Daejung Chemicals (Siheung, Republic of Korea).

### 2.2. Graphene Synthesis and Transfer

Monolayer graphene was grown via CVD on 25  $\mu\text{m}$ -thick copper foils [32] at temperatures close to  $1000\text{ }^{\circ}\text{C}$  using  $\text{CH}_4$  (125 sccm) as a carbon source and  $\text{H}_2$  (100 sccm) as a reactant gas [33]. The PMMA solution was spin-coated onto the graphene at 3000 rpm for 30 s to serve as a supporting layer. The specimen was annealed on a hot plate at  $100\text{ }^{\circ}\text{C}$  for 1 min. The surface of the graphene/copper foils was treated with an  $\text{O}_2$  plasma process (power 150 W, time 30 s) to improve the copper foils' wettability. Subsequently, graphene was separated by etching the Cu foil in an ammonium persulfate solution (2 g ammonium

persulfate in 100 mL deionized (DI) water) for 4 h. Once all of the copper was etched away, only the PMMA/graphene film remained, which was lifted using a glass slide and rinsed twice in DI water. The PMMA/graphene layer was then transferred to a 300 nm SiO<sub>2</sub>/P+Si substrate. Finally, to remove PMMA from the graphene, it was immersed in acetone in two steps: first for 30 min and then for an additional 90 min.

### 2.3. Graphene Patterning, Thermal Cleaning, and Doping

The formation of the graphene-patterned array was achieved using typical photolithography and oxygen plasma etching methods. The graphene was uniformly covered by the PR solution, spinning at 3000 rpm for 30 s, and then baked at 95 °C for 2 min. Subsequently, the sample was exposed to aligner UV light for 15 s, creating a graphene-pattern array with a size of 100 μm × 300 μm. The samples were rinsed with a developer, followed by a rinse with deionized water, and then dried using nitrogen. The exposed graphene regions, not protected by PR, were etched through a reactive ion etching process. The sample was then soaked in acetone for about 30 min to remove the PR from the graphene. As a result, a graphene-pattern array was obtained. To thoroughly remove the PMMA and PR residues that remained after the acetone treatment, the patterned graphene underwent hydrogen annealing (H<sub>2</sub>) at 300 °C for 20 min, ensuring a clean surface [34–36]. Then, the patterned graphene was doped for 12 h to be completely submerged in a hexamethyldisilazane (HMDS) solution. Additionally, the doped specimen was dried with nitrogen gas.

### 2.4. MoS<sub>2</sub> Synthesis on Graphene

To create a vertically stacked MoS<sub>2</sub> heterostructure on patterned graphene, a 0.633 M solution was formulated by mixing 1.0 g of (NH<sub>4</sub>)<sub>2</sub>MoS<sub>4</sub> precursor with 6 mL of dimethyl sulfoxide (DMSO). A multistep coating technique ensured uniform coverage of the precursor solution on the graphene. SiO<sub>2</sub>/Si wafers (with a 300-nm-thick SiO<sub>2</sub> layer) underwent two spin-coating stages: an initial 10 s spin at 500 rpm, followed by a 30 s spin at 2500 rpm. Subsequently, the specimen was annealed on a hot plate at 150 °C for 3 min to evaporate any remaining solvent. A fiber laser with a 1.06 μm wavelength and 20 W output was employed to selectively anneal the precursor layer, thereby synthesizing MoS<sub>2</sub>. The parameters for optimizing MoS<sub>2</sub> synthesis via the laser were as follows: (i) laser power (from 1 W to 20 W), (ii) scan speed (from 10 mm/s to 500 mm/s), and (iii) frequency (from 20 kHz to 200 kHz). After the selective synthesis of MoS<sub>2</sub>, the untreated parts were washed away by immersion in DMSO solvent.

### 2.5. Device Characterization

The I–V characteristics of the device were measured under low-vacuum conditions ( $5 \times 10^{-3}$  Torr) using a probe station connected to a parameter analyzer (4200, Keithley, Cleveland, OH, USA). To confirm the optoelectronic characteristics, the devices were illuminated using a white-light halogen lamp, and the light intensities were measured using a power meter (PM 100d, Thorlabs, Newton, NJ, USA).

## 3. Results and Discussion

Figure 1a,b illustrates a schematic of the graphene/MoS<sub>2</sub>-heterostructure fabrication through laser-based photothermal synthesis, complemented by the corresponding optical-microscopy images for each step. Initially, graphene was synthesized using the conventional CVD method [33,37], which enabled the uniform production of monolayer graphene over a large area. The graphene was then transferred to a SiO<sub>2</sub>/Si wafer using a PMMA supporting layer. Following the removal of the supporting layer, a rectangular graphene pattern (100 μm × 300 μm) was defined using photolithography and reactive ion etching with O<sub>2</sub> plasma [38]. During these transfer and patterning stages, water molecules may be trapped between the graphene and substrate, or contamination from organic compounds may occur. Therefore, the patterned graphene was annealed via a thermal-cleaning process at 300 °C in a hydrogen atmosphere for 20 min. Furthermore, a self-assembled monolayer

(SAM) of HMDS was applied as a buffer layer to the graphene via a dipping process. This layer mitigated unintended doping effects on the graphene and protected the graphene from the subsequent laser-synthesis step. Subsequently, an ammonium tetrathiomolybdate ( $(\text{NH}_4)_2\text{MoS}_4$ ; ATM) precursor solution was spin-coated onto the patterned graphene. Considering the contrasting nature of the graphene pattern (hydrophobic) and  $\text{SiO}_2$  surface (hydrophilic), achieving a uniform precursor coating on this nonuniform surface is challenging. The optimization strategies for these coatings are discussed in Figure 2. After forming a uniform precursor film, we employed a fiber laser ( $\lambda = 1.06 \mu\text{m}$ ) to synthesize the  $\text{MoS}_2$  pattern on the preformed graphene pattern. We chose a fiber laser among the laser sources with various wavelengths because of its low optical absorption in the surrounding materials, such as graphene,  $\text{SiO}_2$ , and Si; however, it has high optical absorption only in the  $(\text{NH}_4)_2\text{MoS}_4$  precursor. Therefore, only the precursor layer could be selectively heated and thermally decomposed into  $\text{MoS}_2$  [39]. In addition, the fiber laser had a low absorption rate in  $\text{MoS}_2$ , even if  $\text{MoS}_2$  was synthesized after the precursor was thermally decomposed; therefore, the laser penetrated the  $\text{MoS}_2$  [23] without thermal damage. This was the key principle for realizing the graphene/ $\text{MoS}_2$  heterostructure by synthesizing  $\text{MoS}_2$  without damaging graphene in the lower layer. More importantly, this direct-synthesis method can realize a vertically stacked layer structure without using a conventional transfer method, thereby fundamentally avoiding problems such as wrinkles or contamination traps at the interface. The optimized laser conditions on the  $\text{SiO}_2/\text{Si}$  substrate were as follows: a laser power of 10.8 W, scan speed of 100 mm/s, and frequency of 20 kHz. Finally, the source and drain were affixed using shadow masks to analyze the electrical properties of the graphene/ $\text{MoS}_2$  heterojunction. Figure 1c shows Raman spectra obtained from each region of the material at an excitation wavelength of 532 nm. The G and 2D peaks were observed at  $\sim 1599 \text{ cm}^{-1}$  and  $\sim 2700 \text{ cm}^{-1}$ , respectively (marked in red). The 2D peak exhibited a sharp, single Lorentzian line shape and was considerably more intense than the G peak, which is a characteristic feature of monolayer graphene. Additionally, the D peak ( $\sim 1360 \text{ cm}^{-1}$ ), which indicates defects and imperfections within the graphene crystal, was barely discernible. The Raman spectra of  $\text{MoS}_2$  synthesized via the laser-based photothermal reaction are shown in blue. Two prominent  $\text{MoS}_2$  peaks,  $E_{2g}$  and  $A_{1g}$ , could be distinctly observed at  $383 \text{ cm}^{-1}$  and  $409 \text{ cm}^{-1}$ , respectively. A Raman characteristic of  $\text{MoS}_2$  is the narrowing of the gap between these two peaks as it transitions from the bulk state to that of a single layer [40,41]. This allowed the determination of the number of  $\text{MoS}_2$  layers present. The gap between these peaks was approximately  $26 \text{ cm}^{-1}$ , confirming the few-layered nature of  $\text{MoS}_2$ . Atomic force microscopy (AFM) analysis has substantiated that the synthesized molybdenum disulfide ( $\text{MoS}_2$ ) exhibits a consistent and uniform film-like structure with a measured thickness of 10 nm. The thickness control of the  $\text{MoS}_2$  film can be achieved through the regulation of solvent concentration and the adjustment of spin-coating velocity. The critical aspect to consider is that to achieve uniform synthesis of  $\text{MoS}_2$  in film form, it is necessary to adjust the laser scanning speed in accordance with changes in the thickness of the precursor film (Supplementary Material Figure S2). Specifically, thicker precursor layers demand a greater amount of photothermal energy for complete thermal decomposition into  $\text{MoS}_2$ , thereby necessitating a reduction in the laser scanning speed. According to previous research results that analyzed the surface of  $\text{MoS}_2$  synthesized using this method, the  $\text{MoS}_2$  yields a root mean square (RMS) surface roughness of 1.15 nm [23]. Interestingly, these major peaks were also maintained in the heterojunction where graphene and  $\text{MoS}_2$  overlapped (green dot in Figure 1b), as evidenced by the green colored Raman spectra. The strength of the D peak was also similar to that of graphene at its initial intensity. For comparison, we prepared a graphene/ $\text{MoS}_2$  control sample in which  $\text{MoS}_2$  was thermally decomposed from the  $(\text{NH}_4)_2\text{MoS}_4$  precursor using thermal CVD, and we analyzed its Raman characteristics. A comparison between the Raman peak of the graphene/ $\text{MoS}_2$  structure synthesized by laser irradiation (marked in green) and that of the graphene/ $\text{MoS}_2$  structure created by thermal chemical vapor deposition (T-CVD) (marked in black) showed that the Raman characteristics of  $\text{MoS}_2$  were similar, whereas those for graphene exhibited

a pronounced difference. When MoS<sub>2</sub> was directly synthesized using general T-CVD, the underlying graphene sustained thermal damage, leading to an amplified D peak and diminished 2D peak. Therefore, our research demonstrates that the laser-based selective thermal-treatment method can be used to directly synthesize MoS<sub>2</sub> layers on a graphene monolayer without causing damage. This mechanism, when paired with other 2D materials that are amenable to thermal decomposition, holds promise for the assembly of diverse heterojunction structures.

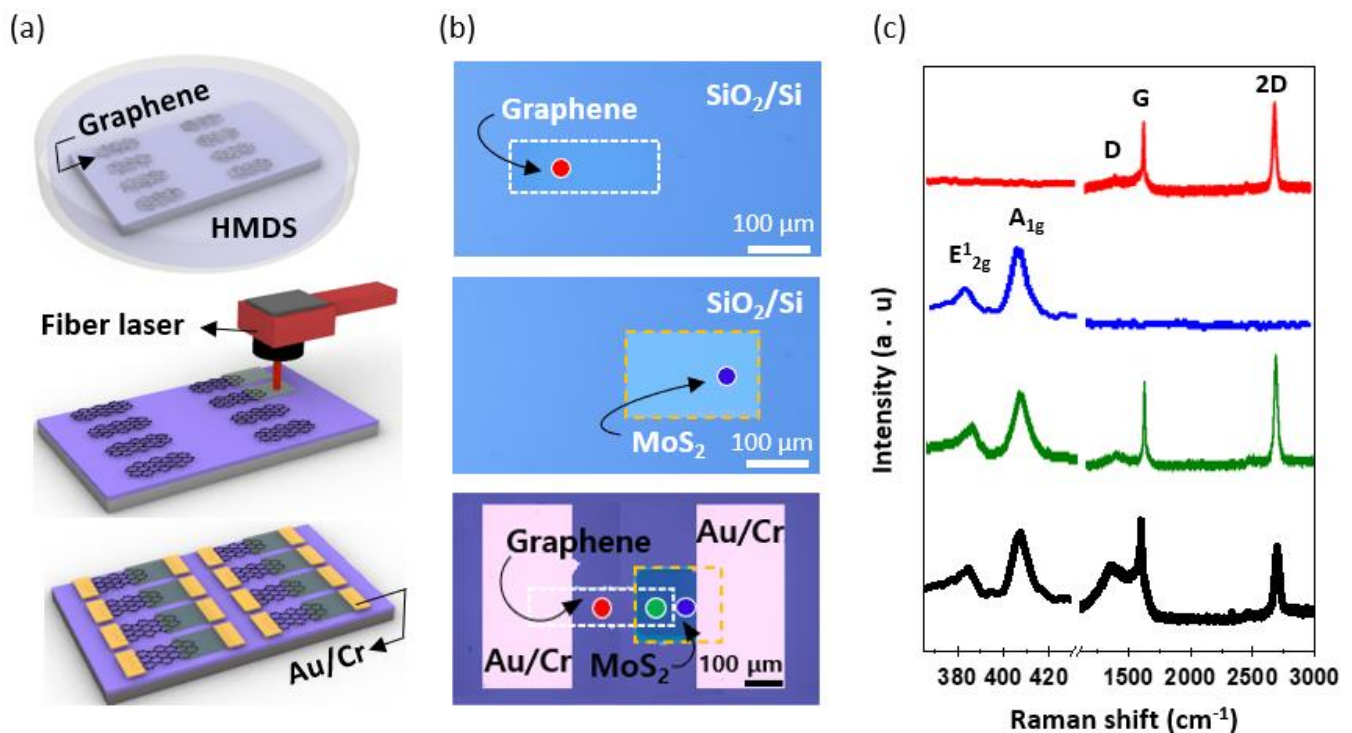


**Figure 1.** (a) Schematic diagram of the device manufacturing process, showing the stacking of MoS<sub>2</sub> on graphene; (b) OM image of patterned graphene, MoS<sub>2</sub>, and a device made by a graphene/MoS<sub>2</sub> heterostructure; (c) Raman spectra for CVD graphene (red), MoS<sub>2</sub> synthesized with a laser (blue), vertically stacked MoS<sub>2</sub> (synthesized with a laser) on graphene (green), and vertically stacked MoS<sub>2</sub> (synthesized with CVD) on graphene (black).

The uniform deposition of the (NH<sub>4</sub>)<sub>2</sub>MoS<sub>4</sub> precursor layer on graphene is essential to demonstrate a MoS<sub>2</sub>/graphene-heterojunction structure. In addition, a uniform and continuous pinhole-free thin film with a large area enabled the fabrication of a device array with a high yield. However, because graphene has a hydrophobic-surface characteristic owing to its unique atomic-crystal [42] structure, a difference was observed in the surface homogeneity between the spin coating of the ATM solution on the SiO<sub>2</sub> substrate and the graphene-transferred SiO<sub>2</sub> substrate, as shown in Figure 2a. To enhance the surface uniformity of the ATM film on graphene, three different solvents—dimethylformamide (DMF) mixed with 2-aminoethanol, a Triton X-100 mixture, and DMSO—were studied. In the case of the SiO<sub>2</sub>/Si substrate, the surface of the wafer was treated with an O<sub>2</sub> plasma process (power 150 W, time 30 s) prior to spin-coating the ATM solution to improve the surface wettability. As shown in the optical-microscopy images in Figure 2b–d, a monotonous and uniform color indicated that the ATM solvent was evenly distributed in all types of samples. However, plasma treatment is not preferred for graphene surfaces because activated oxygen ions can severely damage the graphene, degrading its electrical performance. Therefore, we attempted to overcome this problem by adjusting the interactions between graphene and the solvent. In dissolved ATM solutions, balancing the viscosity and surface tension of the precursor is important. Initially, DMF and 2-aminoethanol were employed as the

solvent and additive [43], respectively. DMF has been used as a common organic solvent to dissolve ATM precursors [39], and amine group-based additive molecules have been used to stabilize ionic thiomolybdate ( $\text{MoS}_4^{2-}$ ) clusters. However, as a result of numerous mixing control experiments between solutions, when DMF + 2-aminoethanol-based solvent was used, obtaining stable coating conditions was difficult as most of the graphene layers rolled after peeling from the substrate as indicated by the arrow in Figure 2e. Although we attempted to use another amine-based additive (*n*-butylamine), a similar phenomenon occurred when the solvent penetrated the substrate and graphene, resulting in delamination. As an alternative, the surface tension of the solution was controlled by adding Triton X-100 surfactant to the ATM solution. As a non-ionic surfactant, the hydrophobic group of Triton-X-100 engaged in interactions with the carbonaceous surface, leading to its adsorption onto the graphene surface. This adsorptive phenomenon enhanced the wettability of the graphene substrate, thereby facilitating a more uniform dispersion of the solvents on its surface [44]. Figure 2f appears to show improved homogeneity; however, complete homogeneity across the graphene surface was not achieved. As a result, the graphene was partially peeled off from the substrate as indicated by arrow. Interestingly, although DMSO is a polar organic solvent similar to DMF, experimental observations indicated that the ATM solution uniformly coated the graphene without causing any damage when DMSO was used as the solvent [45]. Based on previous experimental procedures, it is speculated that the balance between the surface tension of DMSO, the ionic thiomolybdate cluster, and the van der Waals forces [46] between the graphene and  $\text{SiO}_2$  interface may allow for an even coating of the ATM precursor without peeling off the graphene (Figure 2g). Finally, when the ATM solution was spin-coated onto the  $\text{SiO}_2$  substrate, it was confirmed that the DMF, Triton X-100 mixture, and DMSO were homogeneously coated on the surface. However, to spin-coat the graphene-transferred  $\text{SiO}_2$  substrate, it was confirmed that the surface could be coated homogeneously using the DMSO solvent.

The electrical-junction properties of the fabricated graphene/ $\text{MoS}_2$  were investigated. First, an HMDS layer was deposited on the graphene surface to minimize the unintentional doping effect caused by the Cu etchant and supporting polymer during the transfer process of the CVD graphene. That is, the hydrophobic SAM including HMDS suppressed the charge-impurity scattering effect caused by the impurity and simultaneously improved overall uniformity [47,48]. In addition, the HMDS buffer layer prevented damage to graphene from additional processes such as metal deposition [49] and laser annealing. Figure 3a illustrates the HMDS-doped graphene-based back-gate transistor on the Si/ $\text{SiO}_2$  substrate. The HMDS treatment was conducted for 12 h on the graphene transferred onto the  $\text{SiO}_2$ /Si substrate prior to the deposition of the contact electrodes. The Raman spectra of graphene before and after HMDS doping are shown in Figure 3b. The Raman-frequency values of the G and 2D modes were sensitive to charge impurities and strains in graphene, enabling us to confirm the influence of HMDS. The G and 2D peak positions of pure graphene were  $1600\text{ cm}^{-1}$  and  $2695\text{ cm}^{-1}$ , respectively (marked in black); however, after HMDS formation, both peaks shifted down to  $1595\text{ cm}^{-1}$  and  $2686\text{ cm}^{-1}$ , respectively (marked in red). The Raman shift indicated that although the surface of graphene had hydrophobic characteristics, the entire surface was covered well with HMDS because some existing defects or oxidized species in graphene played a role in nucleating the SAM [49]. Moreover, the extracted value of  $\Delta 2D/\Delta G$  was less than 2 [50], which indicates that no effective stress was applied to graphene after HMDS deposition. A comparative assessment of the Fermi energy and carrier mobility of pristine and HMDS-doped graphene is shown in Figure 3c. For the bare graphene, a gate voltage (Dirac point) was observed at 33.1 V. However, after the HMDS-doping process, a pronounced Dirac-point shift to lower gate voltages was repeatedly observed ( $V_G$ : 22.2 V) [48,51–53]. Based on the electronic structure of graphene, the Dirac-point shift may be associated with the change in Fermi energy.

Because of the linear band structure of graphene, the shift in Fermi energy caused by the HMDS dipole can be described as follows [54]:

$$\Delta E = \hbar v_F \sqrt{\pi n (V_2 - V_1)},$$

where  $v_F$  is the Fermi velocity previously reported as  $1.1 \times 10^6$  m/s,  $n$  is the intrinsic carrier density per volt with a typical value of approximately  $7.2 \times 10^{10} \text{ cm}^{-2} \text{ V}^{-1}$ , and  $V_1$  ( $V_2$ ) is the Dirac point of devices without (with) HMDS treatment. The calculation confirmed that the HMDS treatment shifted the Fermi-energy level of graphene by 0.11 eV closer to the vacuum level. The field-effect carrier mobility of graphene was additionally calculated from the maximum slope near the charge-neutrality point, as follows:

$$\mu_{FET} = \frac{L_{ch} g_m}{W_{ch} C_{ox} V_D}$$

where  $L_{ch}$  and  $W_{ch}$  are the channel length and width, respectively,  $g_m$  is  $dI_D/dV_G$ ,  $C_{ox}$  is the gate oxide capacitance per area, and  $V_D$  is the applied drain-source voltage. As plotted in Figure 3c, the hole and electron carrier mobilities of HMDS-treated graphene showed values of  $\sim 450.8 \text{ cm}^2/\text{Vs}$  and  $\sim 297.9 \text{ cm}^2/\text{Vs}$ , respectively. This represents a significant enhancement in mobility compared to bare graphene ( $\mu_{\text{hole}}$ :  $\sim 86.5 \text{ cm}^2/\text{Vs}$  and  $\mu_{\text{elec}}$ :  $\sim 95.4 \text{ cm}^2/\text{Vs}$ ). The electrical properties of MoS<sub>2</sub>, interfaced with graphene, were also analyzed via transfer characteristics (Supplementary Materials, Figure S3). The MoS<sub>2</sub> synthesized via laser based photothermal processing demonstrated comparatively lower electron mobility, ranging from 1 to 5  $\text{cm}^2/\text{Vs}$ , than that synthesized through chemical vapor deposition (CVD) methods, with an observed on/off ratio of  $10^3$ . These moderate properties can be attributed to the fine-grained structure of the laser-synthesized MoS<sub>2</sub>. Determining the electronic band structure of the synthesized graphene/MoS<sub>2</sub> heterostructure is necessary for analyzing its electrical characteristics and understanding its charge-transfer dynamics. The work function of each material was experimentally measured using ultraviolet photoelectron spectroscopy. The work function was calculated as follows [33]:

$$\Phi = h\nu - (E_{SECO} - E_{VB}),$$

where  $h\nu$  is the energy of the incident UV photons (He I line = 21.21 eV),  $E_{SECO}$  is the secondary electron-cutoff energy, and  $E_{VB}$  is the onset of the valence band. As expected, bare graphene exhibited significant fluctuations in the analysis value, ranging from 4.3 eV to 5.2 eV depending on the measurement position, whereas HMDS-doped graphene exhibited a stable value of approximately 4.5 eV. Furthermore, MoS<sub>2</sub> synthesized by laser treatment exhibited a uniform work function of approximately 4.2 eV, which was in good agreement with that of the few-layered MoS<sub>2</sub> [21]. Figure 3f illustrates the band alignment of the graphene/MoS<sub>2</sub> heterojunction, delineated according to the positions of the respective band structures. In a thermal-equilibrium state, the band structure bends at the interface due to the difference in work functions between graphene and MoS<sub>2</sub>, creating a Schottky barrier ( $\Phi_B$ ) and built-in potential ( $V_{bi}$ ) on the semiconductor side. For an applied external bias, the Fermi level of graphene shifted downward during the application of a reverse bias owing to the decrease in negative charges moving toward the graphene, whereas the Fermi level of the n-type MoS<sub>2</sub> shifted upward, as illustrated in Figure 3g. This upward shift of the MoS<sub>2</sub> Fermi level relieved the band bending, leading to a decrease in the built-in potential. Conversely, when a forward bias was applied to the graphene/MoS<sub>2</sub> Schottky junction, the Fermi level of graphene shifted upward, whereas that of the MoS<sub>2</sub> shifted downward. This occurred because more positive charges were localized in the MoS<sub>2</sub> and more negative charges were transported to the graphene, as depicted in Figure 3h. Unlike the scenario under reverse bias, the value of the built-in potential increased during the application of a forward bias. When a reverse bias was applied, the majority carriers of MoS<sub>2</sub> and graphene easily overcame the lowered built-in potential and transferred to

the counter materials beyond the junction. However, in the case of a forward bias, the barrier at the junction was high; therefore, the charges were greatly restricted when moving toward each other. Therefore, owing to the aforementioned charge-transfer dynamics, the graphene/MoS<sub>2</sub> junction, which was MoS<sub>2</sub> directly synthesized on graphene using a laser-assisted methodology, exhibited rectification characteristics that depended on the applied forward-to-reverse bias. However, when MoS<sub>2</sub> was grown via the thermal CVD process on the graphene, the underlying graphene experienced pronounced thermal degradation. These harsh synthesis conditions led to a substantial decline in conductivity, or in certain instances, a failure to establish a Schottky barrier, thereby inhibiting any rectifying behavior, as shown in Figure 3e.

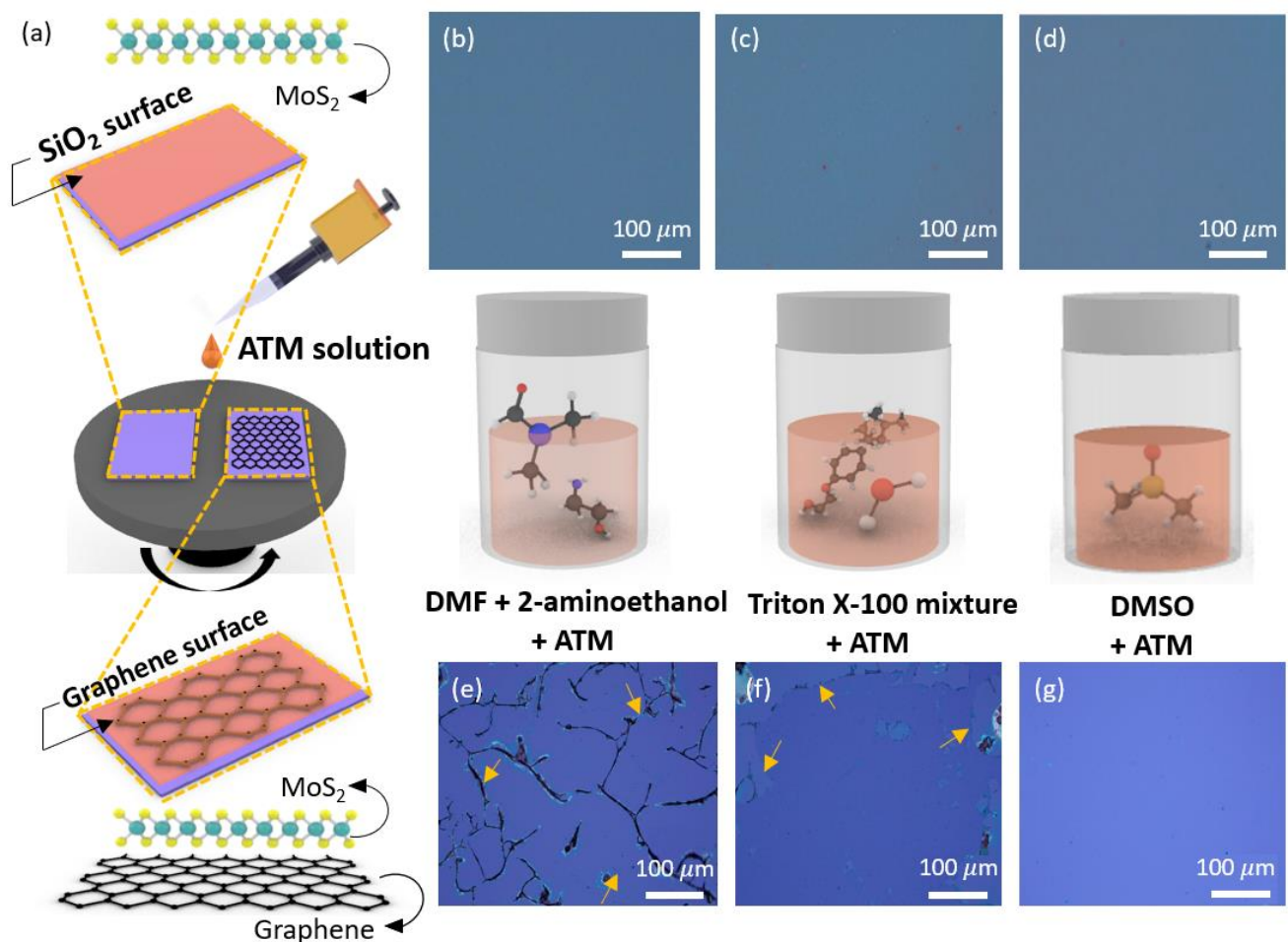


**Figure 2.** (a) Schematic illustration of the coating process for the (NH<sub>4</sub>)<sub>2</sub>MoS<sub>4</sub> precursor on SiO<sub>2</sub> and graphene/SiO<sub>2</sub> surfaces. Optical-microscopy images showing the (NH<sub>4</sub>)<sub>2</sub>MoS<sub>4</sub> precursor spin-coated onto a SiO<sub>2</sub> surface with different solvents: (b) DMF + 2-aminoethanol, (c) Triton X-100 mixture, and (d) DMSO. Optical-microscopy images of the (NH<sub>4</sub>)<sub>2</sub>MoS<sub>4</sub> precursor spin-coated onto a graphene/SiO<sub>2</sub> substrate using the following solvents: (e) DMF + 2-aminoethanol, (f) Triton X-100 mixture, and (g) DMSO.

The developed graphene/MoS<sub>2</sub>-based Schottky junction was characterized in terms of its optical responsiveness to external light by periodically turning the light on and off. To this end, the optoelectronic device employs the configuration mentioned in Figure 1b, wherein the intersection of the graphene and MoS<sub>2</sub> patterns spans an area of 100 μm × 100 μm. Detailed specifications of the device dimensions are described in the Supplementary Materials, accompanied by illustrative schematics. We used a commercial visible-light halogen lamp (FOK-100 W, Fiber Optic Korea Co., Ltd., Cheonan, Republic of Korea) with a peak wave-

length of 650 nm as the light source. As shown in Figure 4a–d, a difference in photocurrent was observed depending on the bias strength even under a consistent light intensity of  $1.92 \text{ mW/cm}^2$ . To clarify, the optoelectronic device we have constructed incorporates two Schottky junctions encompassing both the graphene/MoS<sub>2</sub> junction and MoS<sub>2</sub>/metal electrode junction. We assessed the photocurrent induced in each region utilizing a focused monochromatic laser beam (refer to Supplementary Material, Figure S4). The result of Figure S4 confirmed that the photocurrent generated at the MoS<sub>2</sub>/metal electrode junction was markedly lower than that at the graphene/MoS<sub>2</sub> junction. The dominant mechanisms that influenced the photocurrent in graphene/MoS<sub>2</sub>-based optoelectronic devices were photoconductivity and photogating [55]. The difference in photoconductivity appeared as an increase in the number of free charge carriers owing to photon absorption. Additionally, charge trapping occurred owing to disorders and defects, resulting in differences in photogating. We plotted the change in photocurrent upon light activation against the photocurrent variation in darkness ( $I/I_0$ ), testing two distinct bias voltages under forward and reverse biases. A larger photocurrent is observed in the case of forward bias. This can be considered to be due to the effect of the internal barrier depending on the direction of the applied bias as mentioned in Figure 3.

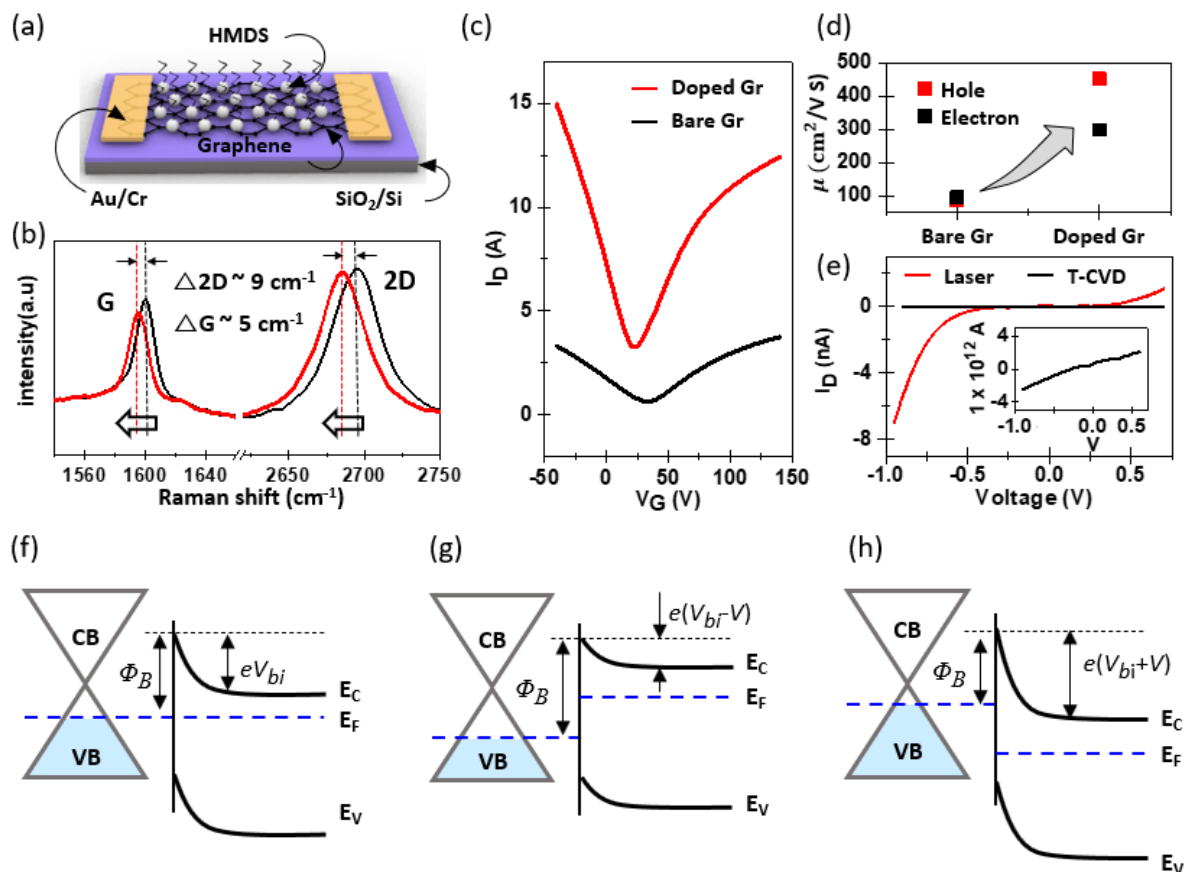


**Figure 3.** (a) Three-dimensional schematic diagram of an HMDS-doped graphene transistor; (b) Raman peak shift of graphene before and after HMDS doping; (c) transfer characteristic of graphene transistor with and without HMDS; (d) comparison of hole and electron carrier mobility before and after HMDS doping; (e) comparison of the rectification characteristics between graphene/MoS<sub>2</sub> produced by the laser method and graphene/MoS<sub>2</sub> produced by the T-CVD method. (Inset: detailed current characteristics of the device fabricated by T-CVD); (f) band diagram of graphene/MoS<sub>2</sub> heterostructure; (g) reverse-bias condition; (h) forward-bias condition.

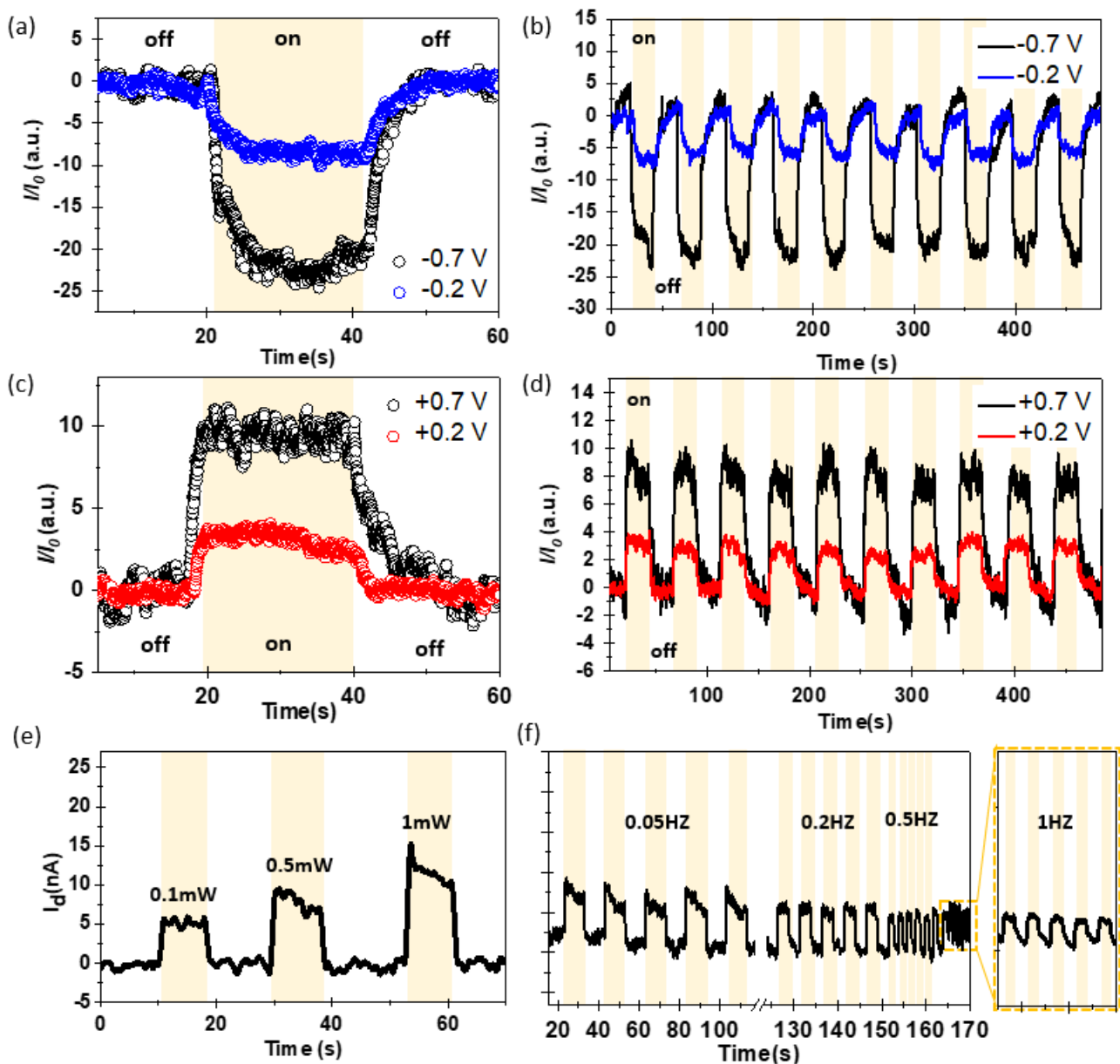


**Figure 4.** (a) Photocurrent characteristic of graphene/MoS<sub>2</sub> heterostructure under reverse bias; (b) cycle stability under reverse bias; (c) photocurrent characteristic of graphene/MoS<sub>2</sub> heterostructure under forward bias; (d) cycle stability under forward bias; (e) current–time characteristic with power of light source; (f) current–time characteristic with frequency.

When considering the rise time ( $\tau_{\text{rise}}$ ) and decay time ( $\tau_{\text{decay}}$ ) of the charge carrier, which represent the duration of charge transfer and production of the maximum output current (ranging between 10 and 90% intensity), respectively, we extracted the following values:  $\tau_{\text{rise}} = 10.3$  s ( $\tau_{\text{decay}} = 8.49$  s) at  $-0.7$  V,  $10.96$  s ( $8.9$  s) at  $-0.2$  V,  $4.6$  s ( $7.26$  s) at  $0.2$  V, and  $6.41$  s ( $7.74$  s) at  $0.7$  V [56,57]. From an on/off photoresponsivity-ratio perspective, the reverse bias exhibited enhanced light reactivity. However, the forward bias demonstrated swifter responsiveness. For a comparative analysis, we fabricated graphene/MoS<sub>2</sub>-based junction devices using the CVD method and evaluated their characteristics. Upon analyzing the photoresponse under the same illumination conditions, it was found that the device fabricated using CVD synthesis exhibited negligible photocurrent generation. A detailed examination of the individual components revealed that the graphene had almost entirely lost its conductivity. These findings suggest that the graphene underwent signif-

ificant damage during the MoS<sub>2</sub> synthesis process (process temperature > 700 °C), which accounts for the absence of the rectifying effect as presented in Figure 3e. The tendency of currents to respond to light was shown to increase monotonically and proportionally as the intensity of the light increased linearly with no evidence of hysteresis (Figure 4e). We also investigated the temporal photoresponse, which indicated the potential of a photodetector, by monitoring the photocurrent under pulsed illumination in the frequency range of 0.05–1 Hz (Figure 4f). The graphene/MoS<sub>2</sub>-based Schottky diode was highly responsive to the incident pulsed light, with excellent stability and reproducibility over multiple cycles.

#### 4. Conclusions

In this study, we introduced a facile approach for the selective synthesis of MoS<sub>2</sub> on graphene by employing laser-based photothermal treatment, which enabled the direct formation of graphene/MoS<sub>2</sub> heterostructures. Notably, this innovative technique offered a means of designing heterostructures from thermally sensitive materials by confining the heat treatment to the intended layer, effectively addressing the challenges that existing T-CVD methodologies cannot overcome. Central to our study is the understanding that the choice of the laser source is crucial. It must efficiently induce the thermal decomposition of the precursor without compromising the structural integrity of the synthesized MoS<sub>2</sub> and graphene. This balance was achieved by harnessing the differential light-absorption rates of the ATM precursor and MoS<sub>2</sub>. Furthermore, we provided solutions for mitigating the surface irregularities introduced by graphene, thereby paving the way for achieving a uniform coating. The introduction of an HMDS buffer layer was a pivotal step that safeguarded the electrical characteristics of graphene throughout the fabrication sequence. Comprehensive evaluation of the electrical properties of the synthesized graphene/MoS<sub>2</sub> heterostructures yielded encouraging results. Although this study did not specifically address contact resistance issues, it expects that the optimization of contact resistance between the two-dimensional semiconductor and the metal electrode could significantly enhance the operational efficiency of the photoelectric device [58–63]. As we venture deeper into the expansive field of this pioneering synthesis technique, we anticipate its widespread adoption and its pivotal role in driving next-generation devices and technologies.

**Supplementary Materials:** The following supporting information can be downloaded at: <https://www.mdpi.com/article/10.3390/nano13222937/s1>, Figure S1: Schematic diagram of Graphene/MoS<sub>2</sub> based optoelectronic device; Figure S2: AFM measurement; Figure S3 Transfer/output characteristics of MoS<sub>2</sub> FET; Figure S4: Photocurrent Comparison between Graphene/MoS<sub>2</sub> and MoS<sub>2</sub>/Cr/Au Junctions; Figure S5: Schematic diagram for manufacturing a CVD type device array; Figure S6: Photo-responsiveness of CVD type device.

**Author Contributions:** M.J.J. and S.-K.H. conceived and performed the experiments. H.Y.J. prepared the materials. J.M. and T.-W.K. analyzed the data. S.B. and S.-K.L. wrote the manuscript. All authors have read and agreed to the published version of the manuscript.

**Funding:** This work was financially supported by a National Research Foundation of Korea (NRF) grant funded by the Korean government (Grant No. 2022R1F1A1072339) and Development of core technologies for advanced measuring instruments funded by Korea Research Institute of Standards and Science (KRISS-2023-GP2023-0012) and the Ministry of Trade, Industry & Energy of Korea (20019508).

**Data Availability Statement:** Data are contained within the article and Supplementary Materials.

**Conflicts of Interest:** The authors declare no conflict of interest.

#### References

1. Sun, Y.; Choi, W.M.; Jiang, H.; Huang, Y.Y.; Rogers, J.A. Controlled buckling of semiconductor nanoribbons for stretchable electronics. *Nat. Nanotechnol.* **2006**, *1*, 201–207. [[CrossRef](#)]
2. Baca, A.J.; Meitl, M.A.; Ko, H.C.; Mack, S.; Kim, H.S.; Dong, J.; Ferreira, P.M.; Rogers, J.A. Printable single-crystal silicon micro/nanoscale ribbons, platelets and bars generated from bulk wafers. *Adv. Funct. Mater.* **2007**, *17*, 3051–3062. [[CrossRef](#)]

3. Yoon, J.; Jo, S.; Chun, I.S.; Jung, I.; Kim, H.-S.; Meitl, M.; Menard, E.; Li, X.; Coleman, J.J.; Paik, U. GaAs photovoltaics and optoelectronics using releasable multilayer epitaxial assemblies. *Nature* **2010**, *465*, 329–333. [[CrossRef](#)]
4. Solís-Fernández, P.; Bissett, M.; Ago, H. Synthesis, structure and applications of graphene-based 2D heterostructures. *Chem. Soc. Rev.* **2017**, *46*, 4572–4613. [[CrossRef](#)]
5. Wassei, J.K.; Kaner, R.B. Graphene, a promising transparent conductor. *Mater. Today* **2010**, *13*, 52–59. [[CrossRef](#)]
6. Azadmanjiri, J.; Srivastava, V.K.; Kumar, P.; Sofer, Z.; Min, J.; Gong, J. Graphene-supported 2D transition metal dichalcogenide van der waals heterostructures. *Appl. Mater. Today* **2020**, *19*, 100600. [[CrossRef](#)]
7. Gong, C.; Hu, K.; Wang, X.; Wangyang, P.; Yan, C.; Chu, J.; Liao, M.; Dai, L.; Zhai, T.; Wang, C. 2D nanomaterial arrays for electronics and optoelectronics. *Adv. Funct. Mater.* **2018**, *28*, 1706559. [[CrossRef](#)]
8. Guan, S.-X.; Yang, T.H.; Yang, C.-H.; Hong, C.-J.; Liang, B.-W.; Simbulan, K.B.; Chen, J.-H.; Su, C.-J.; Li, K.-S.; Zhong, Y.-L. Monolithic 3D integration of back-end compatible 2D material FET on Si FinFET. *npj 2d Mater. Appl.* **2023**, *7*, 9. [[CrossRef](#)]
9. Chung, Y.-Y.; Chou, B.-J.; Hsu, C.-F.; Yun, W.-S.; Li, M.-Y.; Su, S.-K.; Liao, Y.-T.; Lee, M.-C.; Huang, G.-W.; Liew, S.-L. First Demonstration of GAA Monolayer-MoS<sub>2</sub> Nanosheet nFET with 410  $\mu\text{A } \mu\text{m}^{-1}$  I<sub>D</sub> 1V V<sub>D</sub> at 40 nm gate length. In Proceedings of the 2022 International Electron Devices Meeting (IEDM), San Francisco, CA, USA, 3–7 December 2022; pp. 34.35.31–34.35.34.
10. Kang, K.; Xie, S.; Huang, L.; Han, Y.; Huang, P.Y.; Mak, K.F.; Kim, C.-J.; Muller, D.; Park, J. High-mobility three-atom-thick semiconducting films with wafer-scale homogeneity. *Nature* **2015**, *520*, 656–660. [[CrossRef](#)]
11. Tan, L.K.; Liu, B.; Teng, J.H.; Guo, S.; Low, H.Y.; Loh, K.P. Atomic layer deposition of a MoS<sub>2</sub> film. *Nanoscale* **2014**, *6*, 10584–10588. [[CrossRef](#)]
12. Poh, S.M.; Tan, S.J.; Zhao, X.; Chen, Z.; Abdelwahab, I.; Fu, D.; Xu, H.; Bao, Y.; Zhou, W.; Loh, K.P. Large area synthesis of 1D-MoSe<sub>2</sub> using molecular beam epitaxy. *Adv. Mater.* **2017**, *29*, 1605641. [[CrossRef](#)] [[PubMed](#)]
13. Kim, K.S.; Lee, D.; Chang, C.S.; Seo, S.; Hu, Y.; Cha, S.; Kim, H.; Shin, J.; Lee, J.-H.; Lee, S. Non-epitaxial single-crystal 2D material growth by geometric confinement. *Nature* **2023**, *614*, 88–94. [[CrossRef](#)] [[PubMed](#)]
14. Sawka, A. MOCVD growth of gadolinium oxide layers on tubes. *Ceram. Int.* **2023**, *49*, 23835–23843. [[CrossRef](#)]
15. Wofford, J.M.; Nakhaie, S.; Krause, T.; Liu, X.; Ramsteiner, M.; Hanke, M.; Riechert, H.; Lopes, J.M.J. A hybrid MBE-based growth method for large-area synthesis of stacked hexagonal boron nitride/graphene heterostructures. *Sci. Rep.* **2017**, *7*, 43644. [[CrossRef](#)] [[PubMed](#)]
16. Song, Y.; Zou, W.; Lu, Q.; Lin, L.; Liu, Z. Graphene transfer: Paving the road for applications of chemical vapor deposition graphene. *Small* **2021**, *17*, 2007600. [[CrossRef](#)]
17. Zhang, G.; Güell, A.G.; Kirkman, P.M.; Lazenby, R.A.; Miller, T.S.; Unwin, P.R. Versatile polymer-free graphene transfer method and applications. *ACS Appl. Mater. Interfaces* **2016**, *8*, 8008–8016. [[CrossRef](#)]
18. Nagareddy, V.K.; Octon, T.J.; Townsend, N.J.; Russo, S.; Craciun, M.F.; Wright, C.D. Humidity-Controlled Ultralow Power Layer-by-Layer Thinning, Nanopatterning and Bandgap Engineering of MoTe. *Adv. Funct. Mater.* **2018**, *28*, 1804434. [[CrossRef](#)]
19. Zhai, X.; Zhang, R.; Sheng, H.; Wang, J.; Zhu, Y.; Lu, Z.; Li, Z.; Huang, X.; Li, H.; Lu, G. Direct observation of the light-induced exfoliation of molybdenum disulfide sheets in water medium. *ACS Nano* **2021**, *15*, 5661–5670. [[CrossRef](#)]
20. Park, S.; Song, J.; Kim, T.K.; Choi, K.H.; Hyeong, S.K.; Ahn, M.; Kim, H.R.; Bae, S.; Lee, S.K.; Hong, B.H. Photothermally Crumpled MoS<sub>2</sub> Film as an Omnidirectionally Stretchable Platform. *Small Methods* **2022**, *6*, 2200116. [[CrossRef](#)]
21. Park, S.; Park, J.; Kim, Y.-g.; Bae, S.; Kim, T.-W.; Park, K.-I.; Hong, B.H.; Jeong, C.K.; Lee, S.-K. Laser-directed synthesis of strain-induced crumpled MoS<sub>2</sub> structure for enhanced triboelectrification toward haptic sensors. *Nano Energy* **2020**, *78*, 105266. [[CrossRef](#)]
22. Cho, S.; Kim, S.; Kim, J.H.; Zhao, J.; Seok, J.; Keum, D.H.; Baik, J.; Choe, D.-H.; Chang, K.J.; Suenaga, K. Phase patterning for ohmic homojunction contact in MoTe. *Science* **2015**, *349*, 625–628. [[CrossRef](#)]
23. Park, S.; Lee, A.; Choi, K.-H.; Hyeong, S.-K.; Bae, S.; Hong, J.-M.; Kim, T.-W.; Hong, B.H.; Lee, S.-K. Layer-selective synthesis of MoS<sub>2</sub> and WS<sub>2</sub> structures under ambient conditions for customized electronics. *ACS Nano* **2020**, *14*, 8485–8494. [[CrossRef](#)]
24. Goto, T.; Saito, K.; Imaizumi, F.; Hatanaka, M.; Takimoto, M.; Mizumura, M.; Gotoh, J.; Ikenoue, H.; Sugawa, S. LTPS thin-film transistors fabricated using new selective laser annealing system. *IEEE Trans. Electron Devices* **2018**, *65*, 3250–3256. [[CrossRef](#)]
25. Song, M.S.; Park, K.; Lee, K.; Cho, J.W.; Lee, T.Y.; Park, J.; Chae, S.C. Selective Crystallization of Ferroelectric Hf<sub>x</sub>Zr<sub>1-x</sub>O<sub>2</sub> via Excimer Laser Annealing. *ACS Appl. Electron. Mater.* **2023**, *5*, 117–122. [[CrossRef](#)]
26. Xu, M.; Peng, C.; Yuan, Y.; Li, X.; Zhang, J. Enhancing the performance of solution-processed thin-film transistors via laser scanning annealing. *ACS Appl. Electron. Mater.* **2020**, *2*, 2970–2975. [[CrossRef](#)]
27. Lee, J.B.; Lim, Y.R.; Katiyar, A.K.; Song, W.; Lim, J.; Bae, S.; Kim, T.W.; Lee, S.K.; Ahn, J.H. Direct synthesis of a self-assembled WS<sub>2</sub>/MoS<sub>2</sub> heterostructure array and its optoelectrical properties. *Adv. Mater.* **2019**, *31*, 1904194. [[CrossRef](#)]
28. Lee, S.K.; Lee, J.B.; Singh, J.; Rana, K.; Ahn, J.H. Drying-Mediated Self-Assembled Growth of Transition Metal Dichalcogenide Wires and their Heterostructures. *Adv. Mater.* **2015**, *27*, 4142–4149. [[CrossRef](#)]
29. Gong, Y.; Lin, J.; Wang, X.; Shi, G.; Lei, S.; Lin, Z.; Zou, X.; Ye, G.; Vajtai, R.; Yakobson, B.I. Vertical and in-plane heterostructures from WS<sub>2</sub>/MoS<sub>2</sub> monolayers. *Nat. Mater.* **2014**, *13*, 1135–1142. [[CrossRef](#)]
30. Seok, H.; Megra, Y.T.; Kanade, C.K.; Cho, J.; Kanade, V.K.; Kim, M.; Lee, I.; Yoo, P.J.; Kim, H.-U.; Suk, J.W. Low-temperature synthesis of wafer-scale MoS<sub>2</sub>-WS<sub>2</sub> vertical heterostructures by single-step penetrative plasma sulfurization. *ACS Nano* **2021**, *15*, 707–718. [[CrossRef](#)]

31. Pak, S.; Lee, J.; Lee, Y.-W.; Jang, A.-R.; Ahn, S.; Ma, K.Y.; Cho, Y.; Hong, J.; Lee, S.; Jeong, H.Y. Strain-mediated interlayer coupling effects on the excitonic behaviors in an epitaxially grown MoS<sub>2</sub>/WS<sub>2</sub> van der Waals heterobilayer. *Nano Lett.* **2017**, *17*, 5634–5640. [[CrossRef](#)]
32. Losurdo, M.; Giangregorio, M.M.; Capezzuto, P.; Bruno, G. Graphene CVD growth on copper and nickel: Role of hydrogen in kinetics and structure. *Phys. Chem. Chem. Phys.* **2011**, *13*, 20836–20843. [[CrossRef](#)]
33. Im, M.J.; Hyeong, S.-K.; Lee, J.-H.; Kim, T.-W.; Lee, S.-K.; Jung, G.Y.; Bae, S. High uniformity and stability of graphene transparent conducting electrodes by dual-side doping. *Appl. Surf. Sci.* **2022**, *605*, 154569. [[CrossRef](#)]
34. Lee, J.-S.; Choi, Y.-K.; Ha, D.; Balasubramanian, S.; King, T.-J.; Bokor, J. Hydrogen annealing effect on DC and low-frequency noise characteristics in CMOS FinFETs. *IEEE Electron Device Lett.* **2003**, *24*, 186–188.
35. Sun, Y.; Yan, X.; Zheng, X.; Liu, Y.; Zhao, Y.; Shen, Y.; Liao, Q.; Zhang, Y. High on-off ratio improvement of ZnO-based forming-free memristor by surface hydrogen annealing. *ACS Appl. Mater. Interfaces* **2015**, *7*, 7382–7388. [[CrossRef](#)]
36. Ferrah, D.; Renault, O.; Petit-Etienne, C.; Okuno, H.; Hourani, W.; Dipankar, K.; Berne, C.; Bouchiat, V. Photoemission investigation of the graphene surface cleaning by hydrogen/nitrogen plasma. In Proceedings of the 16th European Conference on Applications of Surface and Interface Analysis (ECASIA'15), Granada, Spain, 28 September–1 October 2015.
37. Bae, S.; Kim, H.; Lee, Y.; Xu, X.; Park, J.-S.; Zheng, Y.; Balakrishnan, J.; Lei, T.; Ri Kim, H.; Song, Y.I. Roll-to-roll production of 30-inch graphene films for transparent electrodes. *Nat. Nanotechnol.* **2010**, *5*, 574–578. [[CrossRef](#)]
38. Shin, D.H.; Kim, Y.-j.; Lee, S.-K.; Bae, S.; Ahn, S. Atomically thin alkane passivation layer for flexible and transparent graphene electronics. *Appl. Surf. Sci.* **2023**, *612*, 155695. [[CrossRef](#)]
39. Liu, K.-K.; Zhang, W.; Lee, Y.-H.; Lin, Y.-C.; Chang, M.-T.; Su, C.-Y.; Chang, C.-S.; Li, H.; Shi, Y.; Zhang, H. Growth of large-area and highly crystalline MoS<sub>2</sub> thin layers on insulating substrates. *Nano Lett.* **2012**, *12*, 1538–1544. [[CrossRef](#)]
40. Liang, L.; Meunier, V. First-principles Raman spectra of MoS<sub>2</sub>, WS<sub>2</sub> and their heterostructures. *Nanoscale* **2014**, *6*, 5394–5401. [[CrossRef](#)]
41. Li, H.; Zhang, Q.; Yap, C.C.R.; Tay, B.K.; Edwin, T.H.T.; Olivier, A.; Baillargeat, D. From bulk to monolayer MoS<sub>2</sub>: Evolution of Raman scattering. *Adv. Funct. Mater.* **2012**, *22*, 1385–1390. [[CrossRef](#)]
42. Prydatko, A.V.; Belyaeva, L.A.; Jiang, L.; Lima, L.M.; Schneider, G.F. Contact angle measurement of free-standing square-millimeter single-layer graphene. *Nat. Commun.* **2018**, *9*, 4185. [[CrossRef](#)]
43. Yang, J.; Gu, Y.; Lee, E.; Lee, H.; Park, S.H.; Cho, M.-H.; Kim, Y.H.; Kim, Y.-H.; Kim, H. Wafer-scale synthesis of thickness-controllable MoS<sub>2</sub> films via solution-processing using a dimethylformamide/n-butylamine/2-aminoethanol solvent system. *Nanoscale* **2015**, *7*, 9311–9319. [[CrossRef](#)]
44. Lee, J.-B.; Rana, K.; Seo, B.H.; Oh, J.Y.; Jeong, U.; Ahn, J.-H. Influence of nonionic surfactant-modified PEDOT: PSS on graphene. *Carbon* **2015**, *85*, 261–268. [[CrossRef](#)]
45. Maleski, K.; Mochalin, V.N.; Gogotsi, Y. Dispersions of two-dimensional titanium carbide MXene in organic solvents. *Chem. Mater.* **2017**, *29*, 1632–1640. [[CrossRef](#)]
46. Gao, W.; Xiao, P.; Henkelman, G.; Liechti, K.M.; Huang, R. Interfacial adhesion between graphene and silicon dioxide by density functional theory with van der Waals corrections. *J. Phys. D Appl. Phys.* **2014**, *47*, 255301. [[CrossRef](#)]
47. Lee, B.; Chen, Y.; Duerr, F.; Mastrogianni, D.; Garfunkel, E.; Andrei, E.; Podzorov, V. Modification of electronic properties of graphene with self-assembled monolayers. *Nano Lett.* **2010**, *10*, 2427–2432. [[CrossRef](#)]
48. Lee, W.H.; Park, J.; Kim, Y.; Kim, K.S.; Hong, B.H.; Cho, K. Control of graphene field-effect transistors by interfacial hydrophobic self-assembled monolayers. *Adv. Mater.* **2011**, *23*, 3460–3464. [[CrossRef](#)]
49. Ramadan, S.; Zhang, Y.; Tsang, D.K.H.; Shaforost, O.; Xu, L.; Bower, R.; Dunlop, I.E.; Petrov, P.K.; Klein, N. Enhancing structural properties and performance of graphene-based devices using self-assembled HMDS monolayers. *ACS Omega* **2021**, *6*, 4767–4775. [[CrossRef](#)]
50. Ferrari, A.C.; Basko, D.M. Raman spectroscopy as a versatile tool for studying the properties of graphene. *Nat. Nanotechnol.* **2013**, *8*, 235–246. [[CrossRef](#)]
51. Liu, X.; Qu, D.; Ryu, J.; Ahmed, F.; Yang, Z.; Lee, D.; Yoo, W.J. P-type polar transition of chemically doped multilayer MoS<sub>2</sub> transistor. *Adv. Mater.* **2016**, *28*, 2345–2351. [[CrossRef](#)]
52. Guo, B.; Liu, Q.; Chen, E.; Zhu, H.; Fang, L.; Gong, J.R. Controllable N-doping of graphene. *Nano Lett.* **2010**, *10*, 4975–4980. [[CrossRef](#)]
53. Chowdhury, S.F.; Sonde, S.; Rahimi, S.; Tao, L.; Banerjee, S.; Akinwande, D. Improvement of graphene field-effect transistors by hexamethyldisilazane surface treatment. *Appl. Phys. Lett.* **2014**, *105*, 33117. [[CrossRef](#)]
54. Cernetic, N.; Wu, S.; Davies, J.A.; Krueger, B.W.; Hutchins, D.O.; Xu, X.; Ma, H.; Jen, A.K.Y. Systematic Doping Control of CVD Graphene Transistors with Functionalized Aromatic Self-Assembled Monolayers. *Adv. Funct. Mater.* **2014**, *24*, 3464–3470. [[CrossRef](#)]
55. Han, P.; Marie, L.S.; Wang, Q.X.; Quirk, N.; El Fatimy, A.; Ishigami, M.; Barbara, P. Highly sensitive MoS<sub>2</sub> photodetectors with graphene contacts. *Nanotechnology* **2018**, *29*, 20LT01. [[CrossRef](#)] [[PubMed](#)]
56. Deng, W.; Chen, Y.; You, C.; Liu, B.; Yang, Y.; Shen, G.; Li, S.; Sun, L.; Zhang, Y.; Yan, H. High detectivity from a lateral graphene–MoS<sub>2</sub> schottky photodetector grown by chemical vapor deposition. *Adv. Electron. Mater.* **2018**, *4*, 1800069. [[CrossRef](#)]
57. Lopez-Sanchez, O.; Lembke, D.; Kayci, M.; Radenovic, A.; Kis, A. Ultrasensitive photodetectors based on monolayer MoS. *Nat. Nanotechnol.* **2013**, *8*, 497–501. [[CrossRef](#)] [[PubMed](#)]

58. Schauble, K.; Zakhidov, D.; Yalon, E.; Deshmukh, S.; Grady, R.W.; Cooley, K.A.; McClellan, C.J.; Vaziri, S.; Passarello, D.; Mohney, S.E. Uncovering the effects of metal contacts on monolayer MoS. *ACS Nano* **2020**, *14*, 14798–14808. [[CrossRef](#)] [[PubMed](#)]
59. Shen, P.-C.; Su, C.; Lin, Y.; Chou, A.-S.; Cheng, C.-C.; Park, J.-H.; Chiu, M.-H.; Lu, A.-Y.; Tang, H.-L.; Tavakoli, M.M. Ultralow contact resistance between semimetal and monolayer semiconductors. *Nature* **2021**, *593*, 211–217. [[CrossRef](#)]
60. Leong, W.S.; Luo, X.; Li, Y.; Khoo, K.H.; Quek, S.Y.; Thong, J.T. Low resistance metal contacts to MoS<sub>2</sub> devices with nickel-etched-graphene electrodes. *ACS Nano* **2015**, *9*, 869–877. [[CrossRef](#)]
61. McDonnell, S.; Addou, R.; Buie, C.; Wallace, R.M.; Hinkle, C.L. Defect-dominated doping and contact resistance in MoS. *ACS Nano* **2014**, *8*, 2880–2888. [[CrossRef](#)]
62. English, C.D.; Shine, G.; Dorgan, V.E.; Saraswat, K.C.; Pop, E. Improved contacts to MoS<sub>2</sub> transistors by ultra-high vacuum metal deposition. *Nano Lett.* **2016**, *16*, 3824–3830. [[CrossRef](#)]
63. Sano, K.; Takahashi, T.; Uchida, K. Large variability of contact resistance in Au/Cr/MoS<sub>2</sub> system and its suppression by Cr thinning. *Jpn. J. Appl. Phys.* **2016**, *55*, 36501. [[CrossRef](#)]

**Disclaimer/Publisher's Note:** The statements, opinions and data contained in all publications are solely those of the individual author(s) and contributor(s) and not of MDPI and/or the editor(s). MDPI and/or the editor(s) disclaim responsibility for any injury to people or property resulting from any ideas, methods, instructions or products referred to in the content.